Untangling the sequence of events during the $S_2 \rightarrow S_3$ transition in photosystem II and implications for the water oxidation mechanism

Mohamed Ibrahim[a,1], Thomas Fransson[b,1], Ruchira Chatterjee[c,1], Mun Hon Cheah[d,1], Rana Hussein[a], Louise Lassalle[c], Kyle D. Sutherlin[c], Iris D. Young[c,2], Franklin D. Fuller[e], Sheraz Gul[c], In-Sik Kim[c], Philipp S. Simon[c], Casper de Lichtenberg[d,f], Petko Chernev[d], Isabel Bogacz[c], Cindy C. Pham[c], Allen M. Orville[g,h], Nicholas Saichek[i], Trent Northen[i], Alexander Batyuk[e], Sergio Carbajo[e], Roberto Alonso-Mori[e], Kensuke Tono[j,k], Shigeki Owada[j,k], Asmit Bhowmick[c], Robert Bolotovsky[c], Derek Mendez[c], Nigel W. Moriarty[c], James M. Holton[c,l,m], Holger Dobbek[a], Aaron S. Brewster[c], Paul D. Adams[c,n], Nicholas K. Sauter[c], Uwe Bergmann[o], Athina Zouni[a,3], Johannes Messinger[d,f,3], Jan Kern[c], Vittal K. Yachandra[c,3], and Junko Yano[c,3]

[a]Institut für Biologie, Humboldt-Universität zu Berlin, D-10115 Berlin, Germany; [b]Interdisciplinary Center for Scientific Computing, University of Heidelberg, 69120 Heidelberg, Germany; [c]Molecular Biophysics and Integrated Bioimaging Division, Lawrence Berkeley National Laboratory, Berkeley, CA 94720; [d]Department of Chemistry - Ångström, Molecular Biomimetics, Uppsala University, SE 75120 Uppsala, Sweden; [e]Linac Coherent Light Source, SLAC National Accelerator Laboratory, Menlo Park, CA 94025; [f]Institutionen för Kemi, Kemiskt Biologiskt Centrum, Umeå Universitet, SE 90187 Umeå, Sweden; [g]Diamond Light Source Ltd, Harwell Science and Innovation Campus, OX11 0DE Didcot, United Kingdom; [h]Research Complex at Harwell, Rutherford Appleton Laboratory, OX11 0FA Didcot, United Kingdom; [i]Environmental Genomics and Systems Biology Division, Lawrence Berkeley National Laboratory, Berkeley, CA 94720; [j]Japan Synchrotron Radiation Research Institute, Sayo-cho, Sayo-gun, 679-5198 Hyogo, Japan; [k]RIKEN SPring-8 Center, Sayo-cho, Sayo-gun, 679-5148 Hyogo, Japan; [l]Stanford Synchrotron Radiation Lightsource, SLAC National Accelerator Laboratory, Menlo Park, CA 94025; [m]Department of Biochemistry and Biophysics, University of California, San Francisco, CA 94158; [n]Department of Bioengineering, University of California, Berkeley, CA 94720; and [o]Stanford PULSE Institute, SLAC National Accelerator Laboratory, Menlo Park, CA 94025

Edited by Pierre Joliot, Institut de Biologie Physico-Chimique, Paris, France, and approved April 1, 2020 (received for review January 11, 2020)

In oxygenic photosynthesis, light-driven oxidation of water to molecular oxygen is carried out by the oxygen-evolving complex (OEC) in photosystem II (PS II). Recently, we reported the room-temperature structures of PS II in the four (semi)stable S-states, S_1, S_2, S_3, and S_0, showing that a water molecule is inserted during the $S_2 \rightarrow S_3$ transition, as a new bridging O(H)-ligand between Mn1 and Ca. To understand the sequence of events leading to the formation of this last stable intermediate state before O_2 formation, we recorded diffraction and Mn X-ray emission spectroscopy (XES) data at several time points during the $S_2 \rightarrow S_3$ transition. At the electron acceptor site, changes due to the two-electron redox chemistry at the quinones, Q_A and Q_B, are observed. At the donor site, tyrosine Y_Z and His190 H-bonded to it move by 50 μs after the second flash, and Glu189 moves away from Ca. This is followed by Mn1 and Mn4 moving apart, and the insertion of O_X(H) at the open coordination site of Mn1. This water, possibly a ligand of Ca, could be supplied via a "water wheel"-like arrangement of five waters next to the OEC that is connected by a large channel to the bulk solvent. XES spectra show that Mn oxidation (τ of ∼350 μs) during the $S_2 \rightarrow S_3$ transition mirrors the appearance of O_X electron density. This indicates that the oxidation state change and the insertion of water as a bridging atom between Mn1 and Ca are highly correlated.

photosynthesis | photosystem II | water oxidation | oxygen-evolving complex | X-ray free electron laser

Dioxygen, which supports all aerobic life, is abundant in the atmosphere because of its constant regeneration via photosynthetic water oxidation in plants, algae, and cyanobacteria. The water-splitting chemistry occurs in the oxygen-evolving complex (OEC) of photosystem II (PS II; Fig. 1*A*), which contains a heteronuclear, oxo-bridged Mn_4Ca cluster that catalyzes the reaction:

$$2\,H_2O \rightarrow O_2 + 4\,e^- + 4\,H^+. \quad [1]$$

To allow this reaction to take place, the OEC accumulates four oxidizing equivalents, stepping through intermediates that are referred to as the S-states (S_i, i = 0 through 4) (Fig. 1*B*) (1, 2). These oxidation reactions are driven by the light-induced charge separations in the reaction center of PS II that comprises the chlorophyll *a* moiety P_{680} (most likely consisting of the four excitonically coupled chlorophylls P_{D1}, P_{D2}, Chl_{D1}, and Chl_{D2}) and the neighboring pheophytin molecules $Pheo_{D1/D2}$ as well as the two plastoquinones Q_A and Q_B. The one-electron photochemistry at

Significance

A new bridging oxygen ligand is incorporated between one of the Mn atoms and Ca in the Mn_4Ca cluster during the transition from the one-photon induced S_2 intermediate state to the two-photon induced S_3 state in the catalytic water oxidation reaction in photosystem II. However, the sequence of events leading to this change is not known. Here we report an X-ray crystallography and spectroscopy study at room temperature using an X-ray free electron laser to collect a "molecular movie" of the structural and oxidation state change steps leading to the insertion of this new oxygen bridge, in the 50 μs to 200 ms time scales after photon absorption, which triggers the $S_2 \rightarrow S_3$ state transition.

Author contributions: U.B., A.Z., J.M., J.K., V.K.Y., and J.Y. designed research; M.I., T.F., R.C., M.H.C., R.H., L.L., K.D.S., I.D.Y., F.D.F., S.G., I.-S.K., P.S.S., C.d.L., P.C., I.B., C.C.P., A.M.O., N.S., T.N., A. Batyuk, S.C., R.A.-M., K.T., S.O., A.B., U.B., A.Z., J.M., J.K., V.K.Y., and J.Y. performed research; T.F., R.C., M.H.C., R.H., N.S., T.N., J.M.H., A.S.B., P.D.A., N.K.S., A.Z., and J.M. contributed new reagents/analytic tools; M.I., T.F., R.C., M.H.C., L.L., K.D.S., A. Bhowmick, R.B., D.M., N.W.M., J.M.H., H.D., A.S.B., P.D.A., N.K.S., J.K., and J.Y. analyzed data; and M.I., T.F., R.C., U.B., A.Z., J.M., J.K., V.K.Y., and J.Y. wrote the paper.

The authors declare no competing interest.

This article is a PNAS Direct Submission.

Data deposition: X-ray diffraction datasets and associated models have been deposited in the Research Collaboratory for Structural Bioinformatics (RCSB) Protein Data Bank (https://www.rcsb.org) under PDB ID codes 6W1O for the 0F, 6W1P for the 1F, 6W1Q for the 2F(50 μs), 6W1R for the 2F(150 μs), 6W1T for the 2F(250 μs), 6W1U for the 2F(400 μs), and 6W1V for the 2F(200 ms) data.

[1]M.I., T.F., R.C., and M.H.C. contributed equally to this work.

[2]Present address: Department of Bioengineering and Therapeutic Sciences, University of California, San Francisco, CA 94158.

[3]To whom correspondence may be addressed. Email: athina.zouni@hu-berlin.de, johannes.messinger@kemi.uu.se, vkyachandra@lbl.gov, or JYano@LBL.GOV.

This article contains supporting information online at https://www.pnas.org/lookup/suppl/doi:10.1073/pnas.2000529117/-/DCSupplemental.

First published May 20, 2020.

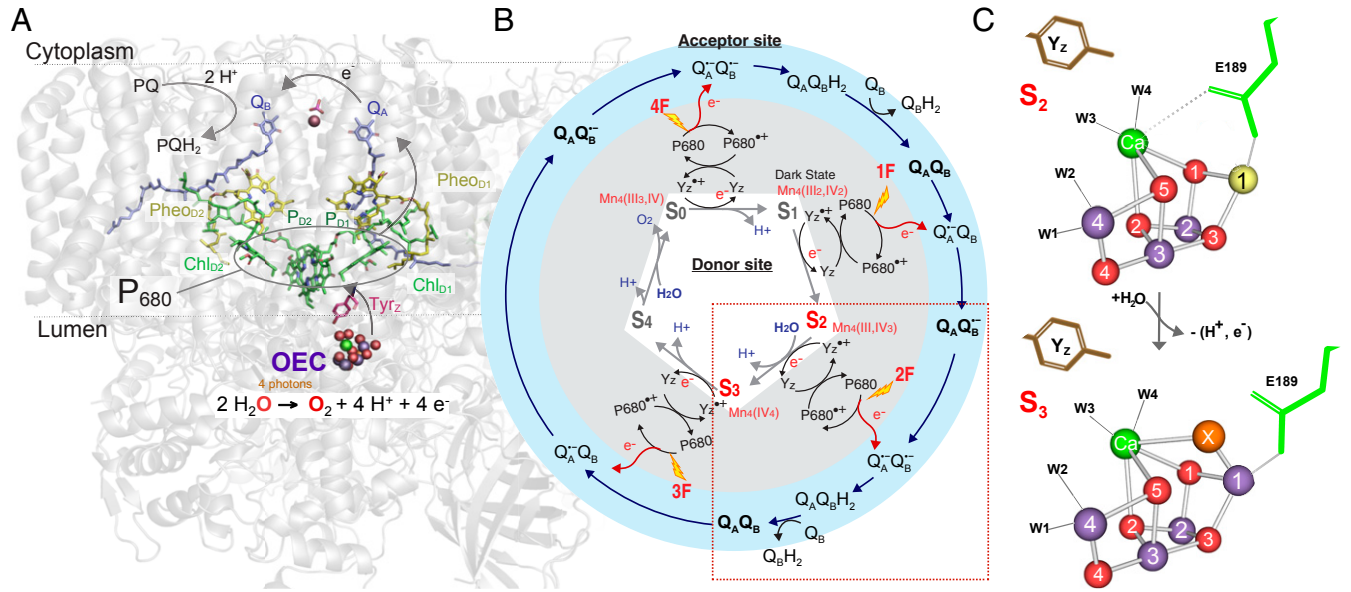

Fig. 1. The $S_2 \rightarrow S_3$ transition in PS II. (*A*) The structure of PS II with the membrane-embedded helices and the large membrane extrinsic regions on the luminal side of PS II are shown as cartoon in gray and in color the main electron transfer components involved in charge transfer (P_{680}, Pheo) and stabilization with the acceptor quinones, Q_A and Q_B, toward the cytoplasm, and Y_Z and OEC with catalytic Mn_4Ca cluster on the donor side at the interface between the membrane and the lumen-bound part of PS II. (*B*) Kok cycle of the water oxidation reaction that is triggered by the absorption of photons (nanosecond light flashes, 1F to 4F) in the antenna and the reaction center P_{680}. The white and gray areas show the redox changes of the OEC (S_1 to S_0) and Y_Z together with the charge separation reactions, while the outer blue circle shows the concomitant acceptor side chemistry of the quinones. The $S_2 \rightarrow S_3$ transition, marked by the red box, is discussed in detail in the main text. (*C*) The structures of the Mn_4Ca cluster, showing the major changes between the S_2 and S_3 states (Mn^{3+} yellow, Mn^{4+} purple, Ca^{2+} green, O red; W1, 2, 3, 4 are water ligands to Mn4 and Ca). The Glu189 residue of the D1 protein as a ligand of Ca moves away during the transition with the insertion of oxygen ($O_X = O^{2-}$ or OH^-) as a new bridging ligand between Mn1 and Ca (adapted from ref. 20).

the reaction center is coupled to the four-electron redox chemistry at the OEC via a redox active tyrosine residue D1-Tyr161, also known as Y_Z. Once four oxidizing equivalents are accumulated (S_4-state), the formation of dioxygen occurs spontaneously and leads to the release of O_2 and the reformation of the S_0-state. At the electron acceptor side of PS II, the electrons created in the charge separation process are transferred to plastoquinone Q_A and subsequently to plastoquinone Q_B. After two light-induced charge separations, the dihydroplastoquinol, Q_BH_2, formed at the Q_B site is replaced by a new plastoquinone molecule (Fig. 1 *A* and *B*) (3, 4).

The significance of the $S_2 \rightarrow S_3$ transition among the four catalytic steps of the Mn_4Ca cluster, is the fact that a water, possibly a substrate, is delivered via a water channel and incorporated into the OEC (Fig. 1 *A* and *B*). Biophysical experiments over the past decades have shown that small perturbations of the OEC can block or severely slow down the rate of this transition, likely by altering the protonation state of the H-bonding network around the OEC. This is caused, for example, by Cl^- depletion (5, 6), substitution of Ca^{2+} by Sr^{2+} in the OEC (7, 8), low temperature (9), and a number of site-directed mutations (10). In addition, there is substantial evidence that the $S_2 \rightarrow S_3$ transition is, by far, the least facile step in the catalytic cycle as it is coupled to the largest reorganization energy, probably due to the water insertion event (11–14).

Since the advent of X-ray free electron lasers (XFELs) there have been efforts to study intermediate states of PS II (15–21). Recently, we reported the crystal structures of all stable intermediates of PS II during the Kok cycle that appear under physiological temperature and two transient time points during the $S_2 \rightarrow S_3$ transition (20). These studies have started unveiling the stepping-stone structures of the catalytic process. The binding of one additional water to the Mn_4Ca cluster was reported in the S_3 state on the basis of XFEL experiments by both Shen and coworkers and by us (19–21). This binding has been predicted by biophysical and computational studies (14, 22–31). However, the chemical form we observed for this newly bound water-derived species differs from the predictions and the initial experimental results; unlike the predicted terminal hydroxo to Mn1 (23, 32) or the experimentally proposed complexed peroxo/superoxo moiety formed together with the O5 bridge (19), we found that the insertion of the new water leads to the formation of an oxo or hydroxo bridge between Mn1 and Ca (Fig. 1*C*) (20). This unexpected binding motif for O_X/O_6 was recently confirmed by Suga et al. (21). Our study also revealed several structural changes that accompany this water insertion event, including the changes in the ligation environment of Ca and metal–metal distances within the Mn_4Ca cluster (20).

However, the exact sequence of changes in the complex $S_2 \rightarrow S_3$ structural rearrangement and the cause for each of the individual steps remains unresolved. Recent time-resolved photothermal beam deflection and Fourier transform infrared (FTIR) experiments have shown that the oxidation of Y_Z by $P_{680}^{\bullet+}$ is followed by proton transfer/release in the $S_2 \rightarrow S_3$ transition, and that only thereafter can the electron transfer from Mn to $Y_Z^{\bullet}$ occur (33, 34). The order of the two other important steps of this transition, oxidation of Mn and insertion of water, is not clear yet, and proposals for either oxidation first or insertion first have been put forward (26, 30, 35–39). Additionally, it was suggested that the cluster undergoes some rearrangement between a "right-open" or "open-cubane" and a "left-open" or "closed-cubane" structure during the $S_2 \rightarrow S_3$ transition (*SI Appendix*, Fig. S1) (40).

The observation from our earlier structural study (20) led us to realize that untangling the sequence of events in the $S_2 \rightarrow S_3$ transition is critical for understanding why one state proceeds to another following a certain pathway, what structural and/or electronic features influence the reaction kinetics, and eventually how is the process fine-tuned. Combining XFEL-based room-temperature serial femtosecond crystallography (SFX) with X-ray

emission spectroscopy (XES) provides a powerful tool to capture and untangle key intermediate structures during this process. Utilizing these methods we report here high-resolution structures and oxidation states of PS II at four time points (50, 150, 250, and 400 μs) during the $S_2 \rightarrow S_3$ transition, probing the kinetics of the electronic and structural changes.

Results and Discussion

Structural Changes during the $S_2 \rightarrow S_3$ Transition. We collected seven different SFX datasets with resolutions ranging from 2.01 to 2.27 Å (*SI Appendix*, Table S1 and Figs. S2–S4). These contained in addition to the dark-adapted (S_1), single-illuminated (S_2), and doubly illuminated (S_3) state (collected 200 ms after the first and second pump laser flash, respectively) four transient state datasets at time points (50, 150, 250, and 400 μs after the second flash) during the $S_2 \rightarrow S_3$ transition. For the analysis of these datasets, we incorporated the ensemble refinement method described by Brewster et al. (ref. 41; also see *Methods*) that takes care of the dynamics of detector metrology and the beam parameters that are fundamental to the XFEL experiment. The structural changes at the donor side, previously observed at 150 and 400 μs at resolutions of 2.20 and 2.50 Å, were reproduced in the current datasets. At the same time, the sequence of structural changes is more evident due to the additional time points (50 μs and 250 μs) and the improved resolution.

Q_A/Q_B Acceptor Quinone Sites. Although the plastoquinones Q_A and Q_B have identical chemical structures, their binding constants inside PS II are quite different, due to their significantly different binding pockets. The binding energies of Q_A and Q_B have been calculated to be −56.1 kcal/mol and −37.9 kcal/mol, respectively (42). The lower binding affinity of Q_B is reflected in our data by the less-well-defined 2Fo-Fc maps and the average B-factor for the quinone head group being about twice as high for Q_B compared to Q_A.

The second flash leads to the reduction of Q_A to Q_A^- and subsequently to the Q_A^- to Q_B^- electron transfer, protonation of Q_B^{2-}, and the exchange of Q_BH_2 with Q_B. Q_A^- formation is clearly seen at 50 μs by the twist of Q_A^- relative to the Q_A position and the ∼0.2 Å decrease of the H-bonding distances to D2-His214 and the backbone nitrogen of D2-Phe261 that is expected due to the increased electronegativity of the semiquinone groups. It is interesting that the isomorphous difference maps around Q_A/Q_A^- change much less than observed for Q_B upon Q_B^- formation (Fig. 2). This suggests that the more rigid protein pocket around Q_A (showing a consistently smaller B-factor compared to the Q_B binding pocket) does not adjust significantly to the reduction of the quinone, which in turn could contribute to the increased reduction potential of Q_A^- compared to that of Q_B^-.

Since the Q_A^- to Q_B and Q_A^- to Q_B^- electron transfers were reported to take place in PS II with time constants of 0.3 to 9 ms (43, 44), the changes observed between 50 μs and 400 μs (Fig. 2 and *SI Appendix*, Fig. S5) reflect the rearrangements of protein/H-bonding due to the reduction of Q_A and the onset of the electron transfer between Q_A^- and Q_B^-. The negligible differences observed in the 2F-0F isomorphous difference maps at the 200 ms time point at the Q_B-site show that the electron transfer from Q_A^- to Q_B^- and the exchange of Q_BH_2 vs a new oxidized quinone of the quinone pool present in the crystal are complete at this stage (exchange with an oxidized quinone is possible due to the presence of a small plastoquinone pool inside the crystal preparations, as shown previously in refs. 18, 20, and 45).

Tyrosine Y_Z (D1-Tyr161)/His190 Site. At the donor site the tyrosine residue, Y_Z (D1-Tyr161), which is located between P_{680} and the OEC (Fig. 1*A*), plays a critical role for electron transfer between these two sites (46–48). Fig. 3 shows the omit maps and models of the Y_Z, D1-His190, and D1-Asn298 residues, overlaid with the 0F(S_1) omit map and structural model. Oxidation of Y_Z after the charge separation at P_{680} has a half-life in the nanosecond to microsecond range (49–51). Therefore, small, but noticeable, changes in this area at 2F(50 μs) correspond to the changes induced by the oxidation of Y_Z after electron transfer to P_{680} which is coupled to the transfer of the phenolic proton to the H-bonding partner His190 (see *SI Appendix*, Fig. S6 for a more detailed view of the H-bonding environment of Y_Z). A tilt of the phenol ring of Y_Z by about 3.5° is observed in comparison to the 0F (S_1) data (Fig. 3). Overall, the largest changes in the electron density are observed at 150 μs after the second flash [2F(150 μs)], implying a significant movement at the His190 and Asn298 side chains. Accordingly, the structural model for the 2F(150 μs) data shows a tilt/shift of the imidazole ring of His190 by ∼0.5 Å in comparison to the S_1 structure and a shift in the side chain of Asn298 of ∼0.3 Å. These changes may be related to subsequent additional protonation state changes in the region of Y_Z-His190-Asn298 that are related to the oxidation of the Mn_4Ca cluster and the insertion of a new water into the O_X position (*Possible Routes for O_X Insertion*). This path has been proposed as a proton transfer pathway by Umena et al. (52). The strong hydrogen bond between the phenolic O-group of Y_Z and the Nτ of His190 makes proton-coupled electron transfer possible upon charge separation (29). In the 250 μs and 400 μs data, D1-His190 and D1-Asn298 have returned to their original positions and a slow relaxation of Y_Z back toward the conformation before charge separation can be observed that reflects the reduction of Y_Z^{ox} by the Mn_4Ca cluster. This process is complete in the fully evolved 2F (S_3) state. The observed changes involving Asn298 in a hydrogen-bond network that is part of a proton transfer pathway away from Y_Z are also in line with mutant studies showing a partial inhibition of the $S_2 \rightarrow S_3$ and $S_3 \rightarrow S_0$ transitions (that both involve proton release) in an Asn298Ala mutant (53). The observed time scale of ∼50 to 200 μs for structural changes around His190 and Asn298 is well in line with proposed time scales for proton transfer events in the $S_2 \rightarrow S_3$ transition (29, 34). It is also worth noting that the changes at His190 are not restricted to the imidazole side chain. They are also connected to a shift of the protein backbone by ∼0.4 Å. This shift in turn is directly connected to a shift of the backbone of the neighboring Glu189 that shows significant side-chain movement in the $S_2 \rightarrow S_3$ transition (discussed below).

OEC. Fig. 4 shows the refined structure around the OEC at each time point, overlaid with isomorphous difference maps relative to the 0F data. Selected atomic distances are shown in Fig. 5*A*. At 50 μs after the second flash, the first observable change in this area involves the Glu189 residue that is 3.8 Å away from the phenolic group of Y_Z. One carboxylate oxygen of this residue ligates to Mn1, while the second carboxylate oxygen has a weak interaction with Ca in the S_1(0F) and S_2(1F) state (2.8 Å), and with W25 (2.6 Å). After the second flash, the Glu189 side chain moves away from Ca but remains as a monodentate ligand to Mn1. The distance to Ca changes from ∼2.8 (1F, S_2) to ∼3.2 Å [2F(50 μs)] (Fig. 5*A*). It shows that the position of the Glu189 carboxylate oxygen facing Ca is highly flexible, and its electrostatic interaction with Ca becomes even weaker during the $S_2 \rightarrow S_3$ transition. We observe that 150 μs after the second flash, Glu189 also moves away from W25 by ∼0.3 Å. This is compatible with the time scale of Y_Z oxidation whereas the subsequent transfer of the positive charge to the OEC did not start yet. It should be noted that changes in side-chain orientation are connected with backbone position changes in both Glu189 and His190 and as they are direct neighbors possibly influence each other (discussed above).

The phenolic oxygen of Y_Z has three neighboring contacts that can form hydrogen bonding interactions: His190, W25, and W4 (*SI Appendix*, Fig. S6). The change in the Glu189–W25 distance suggests that W25 is acting as a proton relay for the subsequent Y_Z protonation step and may subsequently facilitate W3 deprotonation.

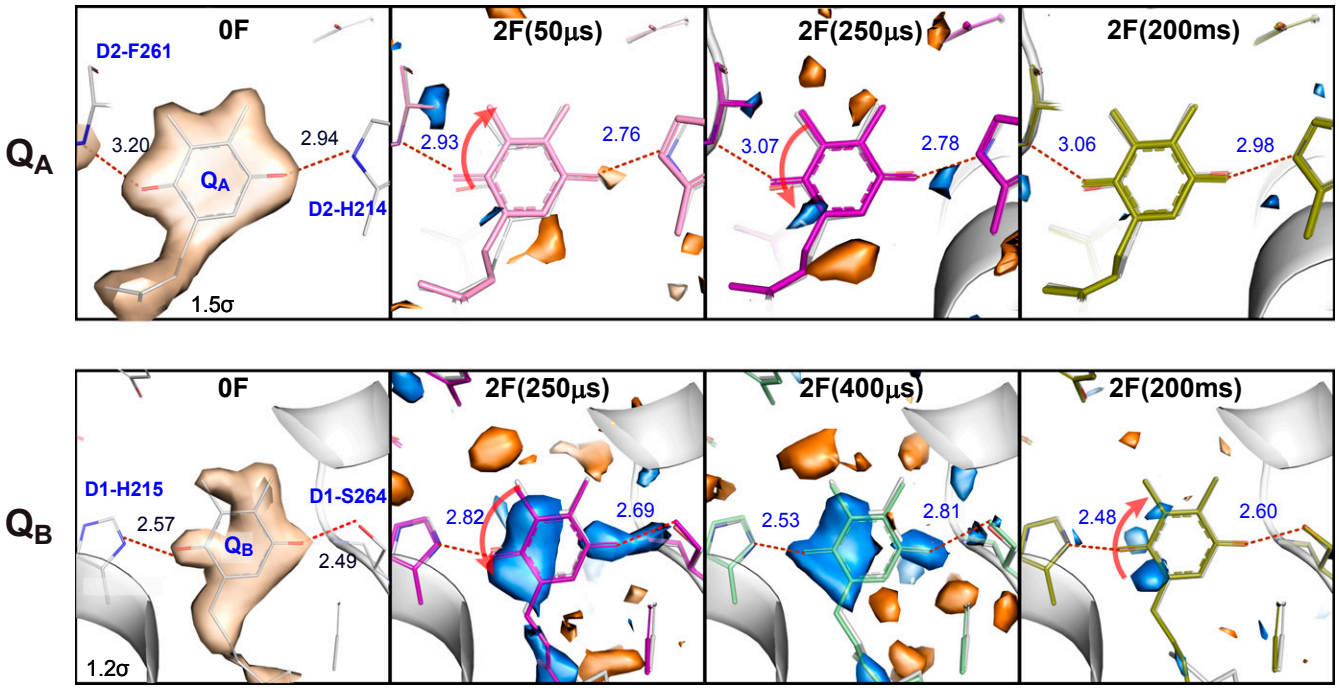

Fig. 2. The acceptor side of PS II. 2Fo-Fc electron density map (contoured at 1.5 σ or 1.2 σ due to different mobility of Q_A and Q_B) of the 0F data, Fo-Fo isomorphous difference maps (contoured at +3 σ [blue] and −3 σ [orange]) of 2F(time point)-0F diffraction data and refined models for 0F and 2F(time point) data in the region of Q_A (*Top*) and Q_B (*Bottom*) on the acceptor side of PS II. Red arrows indicate movement of the quinone head group. The changes at Q_A are observable at the earliest time point (50 μs), while Q_B exhibits constant difference features (due to the presence of the reduced semiquinone) in all time points (see also *SI Appendix*, Fig. S5). Changes in both the Q_A and Q_B regions are much smaller at 200 ms. This is expected as the electron is transferred from Q_A to Q_B within several hundreds of microseconds and then after Q_B took up two redox equivalents it is replaced in the millisecond time scale with an oxidized quinone of the quinone pool present in the crystal.

However, we cannot exclude an alternative scenario, where W4 is the proton relay. In both scenarios, moving of Glu189 away from both Ca and W25/W4 could allow its hydrogen-bonding interaction with the newly inserted O_X in the S_3 state. The current data suggests that Ca could shuttle water molecules between the W3, W4/W25 positions, and the next water molecule. This will be discussed in more detail below.

In the isomorphous difference map (Fig. 4 *A* and *B*), changes in the metal positions at the OEC are already noticeable (albeit weak) at 50 μs and the metal distance changes can first be modeled in the 2Fo-Fc map at 150 μs after the second flash; the elongation of the Mn1–Mn4 distance from ∼4.8 to 5.2 Å (Fig. 5*A*) is observed as positive density appearing adjacent to Mn1 and Mn4 in Fig. 4. It suggests that a slight expansion (∼0.4 Å) of the OEC occurs during the transition from the S_2 to the S_3 state. Interestingly, that expansion seems to reach its maximum value around 250 to 400 μs and a small contraction is observed upon the completion of the S_3 formation. We reported in our previous study that the additional oxygen (O_X, as oxo or hydroxo) is inserted as a bridging oxygen between Mn1 and Ca (20). Following the Mn1–Mn4 elongation, the O_X density starts to appear as a positive feature in the isomorphous difference electron density (Fig. 4 *A* and *B*) between O5 and Mn1 at 150 μs. Likewise, in the omit map (Fig. 4*C*), the presence of O_X becomes visible at the 150 μs time point with ∼30% peak height (Fig. 5*C*), and its intensity reaches nearly maximum around 400 μs at a normalized level of about 60 to 70% of the value obtained for omitting O2 from the OEC (*Methods*), which corresponds to the calculated S_3 state population in this state (*SI Appendix*, Table S2). At this time point, the OEC structure is very similar to that of the stable intermediate S_3 state, indicating that in most of the PS II centers the changes at the OEC are complete around this time point. As discussed later, the O_X insertion kinetics matches favorably with the Mn oxidation kinetics obtained from the $K\beta_{1,3}$ XES (discussed below and see Fig. 5 *B* and *C*).

The presence of a closed-cubane OEC structure has been proposed in the water insertion process during the $S_2 \rightarrow S_3$ transition referred to as a carousel or pivot mechanism (36, 54). These proposals are based on the observation that there are two S_2 states (high-spin and low-spin forms) often detected by electron paramagnetic resonance (EPR), and some theoretical studies predict their structures to have an open- and closed-cubane motif, respectively (25, 40) (see also *SI Appendix*, Fig. S1). In these mechanisms, the water insertion is accompanied by the rearrangement of the OEC at the open coordination site of Mn4 through the shift of O5 to form a closed-cubane motif, prior to the formation of the complete S_3 form. This proposal leads to a flipping of bonds so that the original O5 ends up in the O_X position. Our current data, collected at pH 6.5 and room temperature, show that the Mn3–Mn4 distance remains constant at around 2.7 to 2.8 Å through the $S_2 \rightarrow S_3$ transition (Fig. 5*A*), implying that the cluster maintains a di-μ-oxo configuration with the Mn4–O5–Mn3–O4 moiety anchored by the Glu333 residue forming a bidentate bridge to Mn3 and Mn4. Thus, we did not observe a closed cubane-like structure in the time-point data. The most straightforward interpretation of this is that the formation of such a closed-cubane structure is not necessary during the $S_2 \rightarrow S_3$ transition at room temperature and neutral pH. We, however, note that we may not be able to detect such species, if 1) it is formed and decays before our first time point (50 μs), 2) it is short-lived due to fast formation and decay kinetics, or 3) its fraction is for other reasons 10% or less at each time point. Recent theoretical studies have shown that both forms of the S_2 state structure, the high- and low-spin forms, can be rationalized by an open-cubane structure (37, 55).

While the Mn3–Mn4 distance remains constant, the Mn4–Glu333 distance changes noticeably (Fig. 5*A*). It shortens by ∼0.2

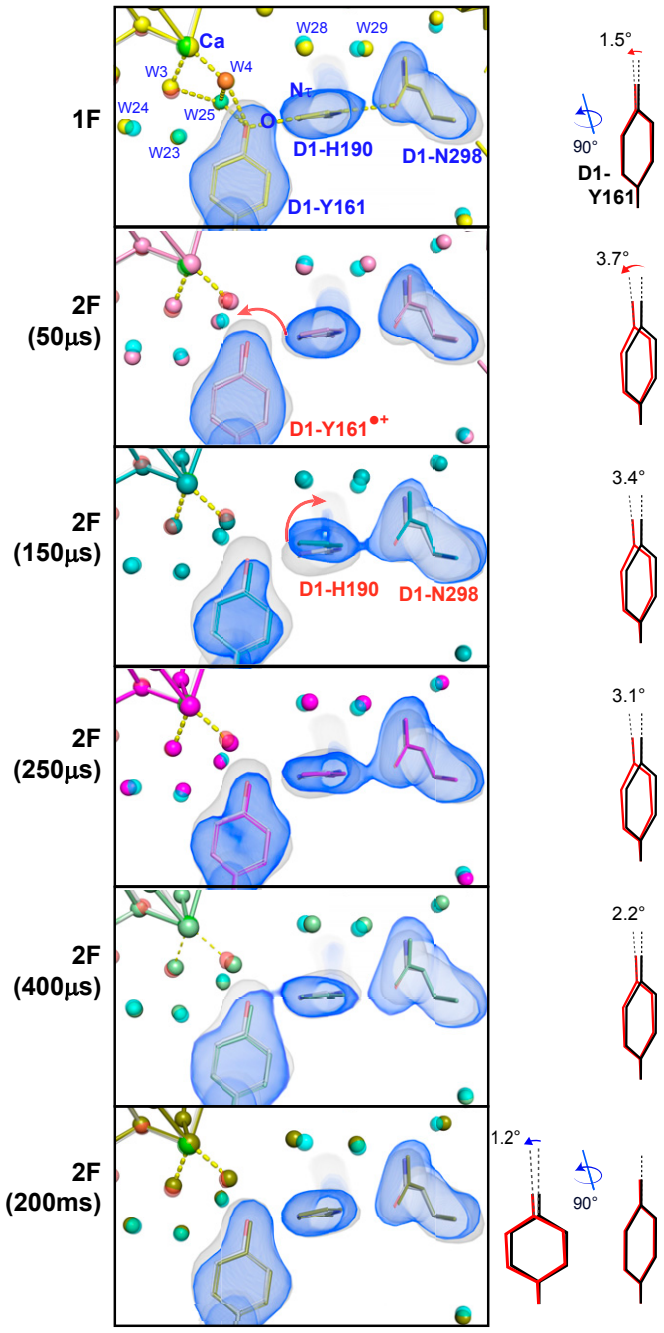

Fig. 3. Fo-Fc electron density omit map of the 0F data (gray) and model (gray) overlaid with the Fo-Fc omit maps (blue) and the models for 1F (yellow) and 2F time points (50 µs: pink; 150 µs: cyan; 250 µs: magenta; 400 µs: green; 200 ms: olive) in the region of D1-Tyr161 (Y_Z). D1-Tyr161, D1-His190, and D1-Asn298 (which were omitted for map generation) are shown together with the Ca of the Mn_4Ca cluster. The tilt angle of the Tyr phenol ring with respect to the 0F structure (black) is shown at the right for each state (red). Within 50 µs the electron is transferred from Y_Z to $P_{680}^{\bullet+}$ as seen by the change in electron density around Y_Z. At 150 µs, Y_Z, D1-His190, and D1-Asn298 all move away from the Mn_4Ca cluster, indicating H-bonding changes that could be connected to proton transfer processes. In the 250-µs data, D1-His190 and D1-Asn298 are back in their original positions and from there onward Y_Z/Y_Z^{ox} slowly returns to the position prior to the light flash, reflecting the reduction of Y_Z^{ox} by the Mn_4Ca cluster.

Å between 0F and 1F, likely reflecting the oxidation of Mn4 from Mn(III) to Mn(IV) upon the $S_1 \rightarrow S_2$ transition. During the transient states between the S_2 and S_3 states, the Mn4–Glu333 distance increases again from 1.8 Å to 2.2 Å and then shortens to be ∼1.9 Å in the stable S_3 state. Similarly, the elongation of Ca–W3 and Mn4–W2 distances is visible slightly above the noise level. The variation in the Mn4–Glu333 distance could be related to the water-insertion event (*SI Appendix*, Fig. S1), either from the Ca-bound W3 site or from the Mn4-bound W2 site via O5 to O_X. Another cause for the change in this distance could be that the movement of the Mn4–Mn3 moiety (necessary for the expansion of the cluster) precedes a change of the Glu333 position and that Glu333 is relaxing into its new position with some delay. Although we cannot exclude other processes happening around Mn4, an involvement of waters bound to Mn4 in the O_X insertion would require the presence of a closed-cubane structure as an intermediate. As our data do not support the presence of such a closed-cubane structure in any of the time points, other water insertion routes seem more likely (discussed below).

Another important aspect of the OEC structure during the $S_2 \rightarrow S_3$ transition is the nature of the inserted O_X (O6 in ref. 21), that is, whether O_X is protonated or not, and the nature of its interaction to O5 that is located in its vicinity. The O5–O_X distance or Mn1–O_X distance becomes detectable in the refined structure at 150 µs after the second flash, and the O5–O_X and Mn1–O_X distances were found to be 1.9 ± 0.14 Å and 1.7 ± 0.25 Å, respectively. In the final S_3 form, the distances are 2.2 ± 0.25 Å for O5–O_X and 1.8 ± 0.18 Å for Mn1–O_X. Error bars on these distances given here and displayed in Fig. 5*A* were calculated by generating 100 perturbed sets of structure factors for each structure using END/RAPID (56), refining the structural model separately against these, and calculating the SD for each bond of interest from the ensemble of structures obtained (details in *SI Appendix*). While the observed distances seem to indicate a transient shortening of Mn1–O_X and elongation of O5–O_X during the formation of S_3 (Fig. 5*A*), we cautiously state that within the error at the current resolution one cannot be conclusive about the changes. However, one can speculate that these distance changes might reflect changes of the protonation state at the O_X site after the water insertion and the possible subsequent proton transfer processes described above. Interestingly, an elongation of the distance between W25 and Glu189 is visible 150 to 250 µs after the second flash (*SI Appendix*, Fig. S6), indicating a weakening of the H-bonding interaction between them. This change could be coupled to the formation of a H-bonding interaction between O_X and Glu189.

Suga et al. (19) initially reported 1.45 Å for the O6($_X$)–O5 distance and proposed a peroxide intermediate, which requires Mn reduction. This is not consistent with the Mn oxidation state assignment in the S_3 state (Fig. 1*B*) (57). Our recent study (20) on all of the S-state intermediates at ∼2 Å resolution at room temperature reported 2.0 to 2.1 Å for the O5–O_X distance in the S_3 state, and the changes as a function of time between S_2 and S_3 from this study (as described above) rule out the presence of a peroxide intermediate at any point in the $S_2 \rightarrow S_3$ transition or the S_3 state. Suga et al. have recently revised their distance estimates to 1.9 Å (21), based on data from frozen crystals. As described in the previous paragraph, a detailed estimation of the individual error for each atomic distance is necessary. The 1.9 Å distance reported in ref. 21 falls at the lower end of our range for the O5–O_X distance.

In order to evaluate if differences in beam conditions (especially pulse length and beam size) could have an influence on the data reported, we collected data at the SPring-8 Ångstrom Compact free-electron LAser (SACLA) (58, 59) (see *SI Appendix* for details) in addition to our measurements at the Macromolecular Femtosecond Crystallography instrument (60) at the Linac Coherent Light Source at SLAC (LCLS) (61). XES and X-ray diffraction data were collected at both facilities with the difference that the pulse length was 7 fs at a beam size of 2 µm × 2.5 µm and the pulse energy was 0.3 mJ at SACLA, instead of 35 fs and 2 mJ and a beam diameter of ∼3 µm at LCLS. The obtained 2F (S_3)

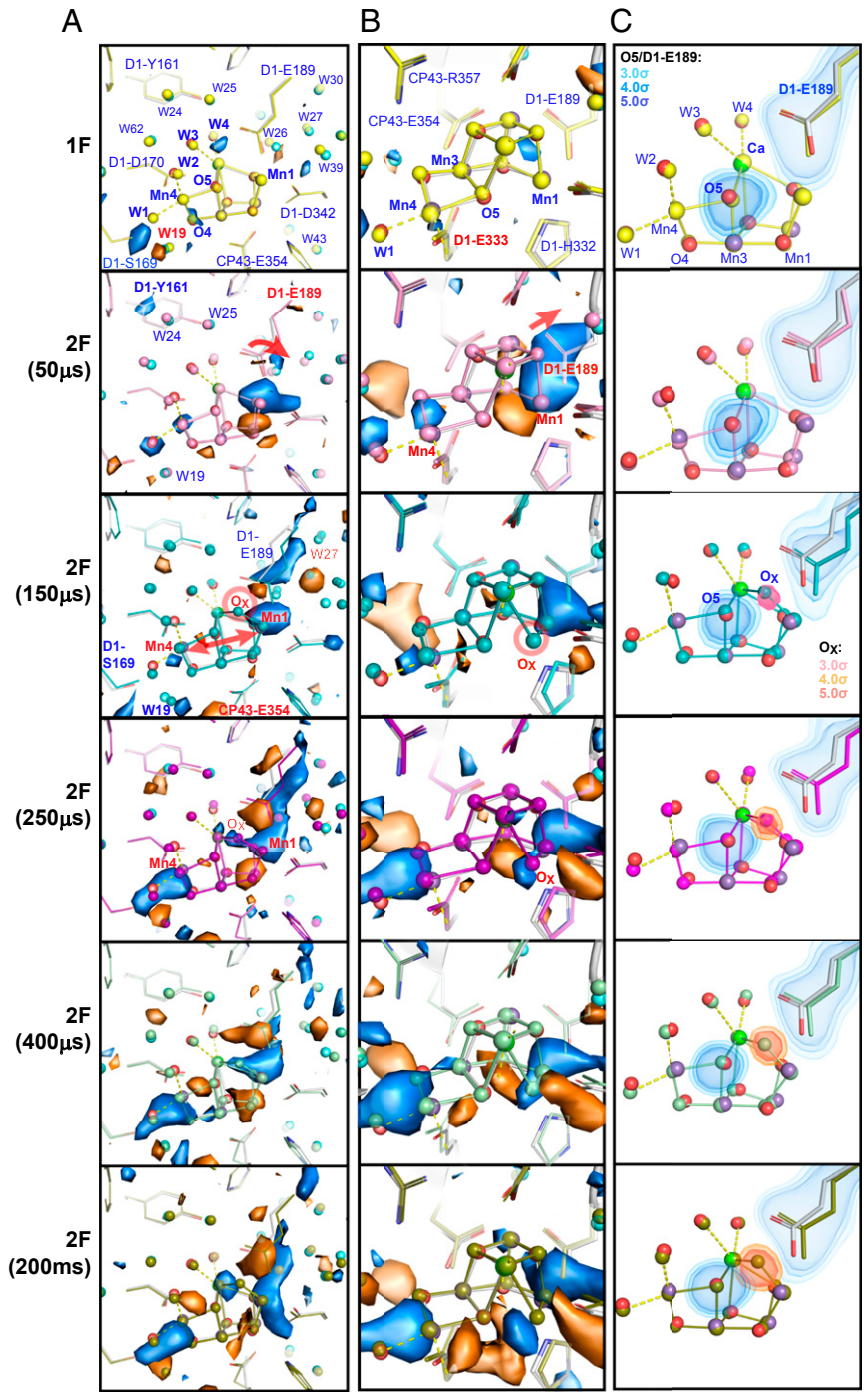

Fig. 4. Structural changes at the OEC in the $S_2 \rightarrow S_3$ transition. (*A* and *B*) Fo-Fo isomorphous difference maps (± 3 σ in blue and orange) of 1F-0F and 2F(time point)-0F datasets in the region of the OEC in two different views for monomer I. (*C*) Fo-Fc omit maps obtained upon separately omitting D1-Glu189 (blue), O5 (blue), and O_X (red), respectively. The dark-state structure is shown as a ball and stick model (carbons in gray, nitrogens in blue, oxygens in red, unbound waters in cyan) overlaid with refined models for various illumination conditions indicated in the left margin. The 1F-0F (S_2-S_1) isomorphous difference map does not feature any significant changes at the OEC (except the disappearance of W20, not shown here but see ref. 20, and the concomitant change in position for W19). At 50 µs the movement of Glu189 away from Ca is seen, followed by Mn1–Mn4 moving apart and O_X binding between Mn1 and Ca from 150 µs onward. The omit maps show the shift of Glu189 starting at 50 µs and more dominantly at 150 µs, while the O_X density appears in the maps starting at 150 µs. While there are slight differences in the two PS II monomer sites (monomer I and II), the overall trend is the same on both sites.

structure from SACLA was refined to 2.4 Å resolution and isomorphous difference densities for the 2F-0F data showed features similar to the ones obtained from data collected at LCLS (*SI Appendix*, Fig. S7*A*). Likewise, the XES data obtained for the 2F state are similar to data collected at LCLS (*SI Appendix*, Fig. S7*B*). From this comparison, we conclude that the different X-ray parameters do not lead to differences in the reported data within the noise level of these measurements and hence cannot be the cause for differences in the distances (19, 21).

Kinetics of the Mn Oxidation State Changes during the $S_2 \rightarrow S_3$ Transition. To investigate the correlation of the O_X insertion between Mn1 and Ca with the Mn(III) to Mn(IV) oxidation state changes of Mn1 during the $S_2 \rightarrow S_3$ transition, we analyzed the first-moment changes of the XES $K\beta_{1,3}$ peak (Fig. 5 *B* and *C* and *SI Appendix*, Fig. S8). Fig. 5*B* shows the Mn $K\beta_{1,3}$ XES first moment of crystal and solution samples at each flash state. Within the error, the XES first moments of the crystal and solution samples behave similarly, confirming that the efficiencies of the S-state transition are comparable between both sample types. The change in the $K\beta_{1,3}$ first-moment energy during the $S_2 \rightarrow S_3$ transition is shown for solution samples in Fig. 5*C*. If single exponential kinetics are assumed, the time constant, τ, of the oxidation state changes under the current experimental condition is ~350 µs (*SI Appendix*, Fig. S9).

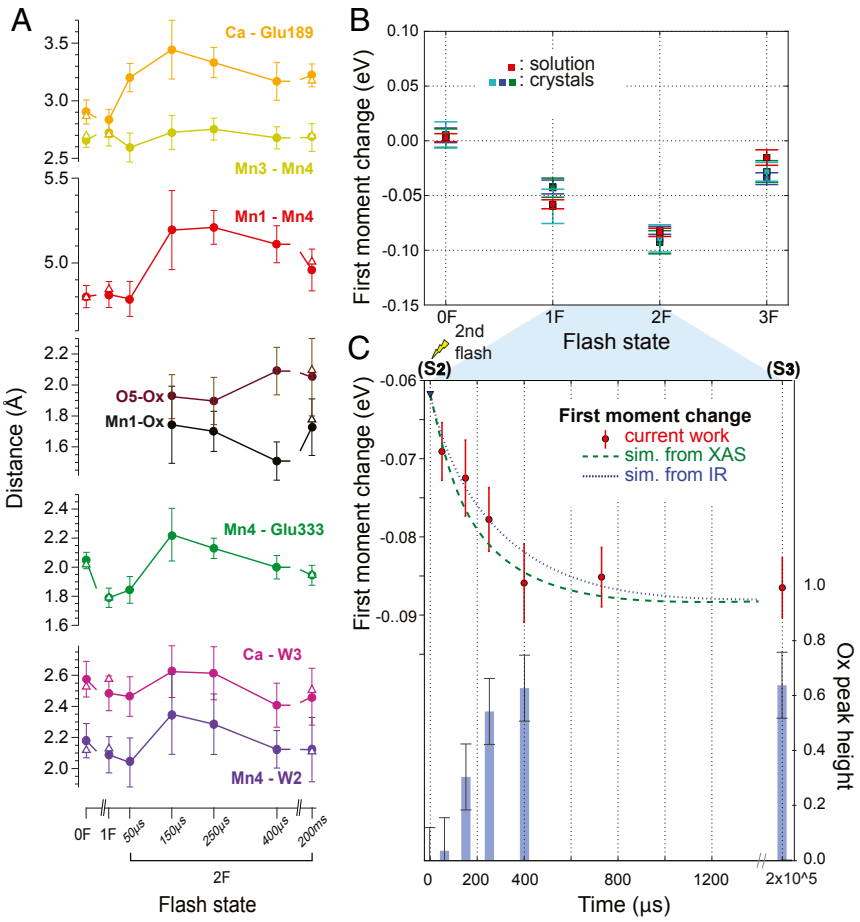

Fig. 5. Changes during the $S_2 \rightarrow S_3$ transition. (*A*) Distance changes for selected bond lengths of 0F, 1F, 2F, and the time points between 1F and 2F, with error bars estimated by generating 100 randomly perturbed datasets, re-refining, and reporting the resulting SD, as described in *SI Appendix*. Open triangles represent values obtained in our previous study for the S_1 (0F), S_2 (1F), and S_3 (2F 200 ms) states (20); values are for monomer I. (*B*) $K\beta_{1,3}$ Mn XES first moment changes of PS II crystals (three independent experiments) and solutions at each flash. All datasets are shifted to overlap for the first moment of the S_1 state. (*C*) $K\beta_{1,3}$ Mn XES first moment changes (red circles) after the second flash. The error bars (red vertical lines) for the XES data are estimated from the standard distribution of 1,000 iterations of randomly dividing all spectra in a dataset into two groups and calculating first moments for each group (75). The S-state populations estimated for our PS II solution samples (*SI Appendix*, Table S2) were taken into account to generate the dashed and dotted lines that show the predicted first moment shift based on time constants from IR (at 10 °C, with *T. elongatus*; ref. 29) and XAS (at room temperature with spinach; ref. 62) studies, respectively (*SI Appendix*). In the same panel, the increase of the O_X omit density in the crystal structure is shown as a histogram (blue bars). To obtain error bars for the O_X omit density, oxygen atom O2 was omitted from the OEC structure, and the SD of the O2 omit density over all datasets in both monomers was used for estimation.

The first-moment trend obtained from the current experiment falls well within the range of the kinetic data reported from time-resolved infrared (IR) and time-dependent X-ray absorption spectroscopy (XAS) studies (29, 62). The expected kinetic traces based on time constants obtained from the IR and XAS studies using our experimentally determined miss and double-hit parameters and S-state population for the 1F solution samples (*SI Appendix* and *SI Appendix*, Table S2 and Fig. S9) are also shown in Fig. 5*C*. We note that the degree of uncertainty in the IR and the XAS data has not been reflected in the simulated lines. Also, the differences among the three experiments, if any, would arise from the differences in the species (plants vs. thermophilic cyanobacteria), temperature (room temperature vs. 10 °C), and the sensitivity of each method to a certain part of the enzyme (metal vs. ligands).

Using IR measurements (at 10 °C, with *Thermosynechococcus elongatus*), Sakamoto et al. (29) described the $S_2 \rightarrow S_3$ process with three phases with time constants: $\tau_1 = 13$ µs, $\tau_2 = 104$ µs, and $\tau_3 = 352$ µs (see blue dotted line in Fig. 5*C* for a plot using only τ_2 and τ_3). They interpreted the first phase to reflect changes in the H-bond interaction of the $Y_Z^{\bullet}$ with a COO^- group, resulting in a lag phase before inititiation of Y_Z rereduction, while the second phase was assigned to changes in the water network and the COO^- groups around the Mn_4Ca cluster due to the rearrangement of the water molecules interacting with $Y_Z^{\bullet}$. The third phase was proposed to reflect the proton release coupled with oxidation of the Mn_4Ca cluster. In the second phase, they suggested that the W3 water moves to the open coordination site of Mn4 or Mn1 in the S_2 state, which could be coupled with internal proton transfer. The XAS study by Zaharieva et al. (62) (at room temperature with spinach), which directly probes Mn, showed that the $S_2 \rightarrow S_3$ process can be fit with two time constants, a very fast transition with a time constant of ~26 µs (τ_1) followed by a slow one (τ_2) with 317 µs (see green dashed line in Fig. 5*C*). Based on the kinetic H/D isotope effect, it was proposed that the fast phase of the $S_2 \rightarrow S_3$ transition is connected to proton release to the bulk and the ~300-µs phase involves a proton-coupled electron transfer and oxidation of the Mn_4Ca cluster.

The oxidation state change from our XES data and those derived from the earlier IR and XAS experiments nearly coincide with the increasing intensity of O_X from crystallography during the $S_2 \rightarrow S_3$ transition shown as a histogram in Fig. 5*C*. This indicates that the kinetics of water insertion and Mn oxidation are highly correlated within the error limits of our current data (*SI Appendix*, *Supplementary Discussion* and Fig. S9). In order to resolve the question of "water binding first" or "Mn oxidation first," XES and diffraction data from earlier time points within the $S_2 \rightarrow S_3$ transition with better signal/noise level will be required.

Water Dynamics during the $S_2 \rightarrow S_3$ Transition. In the current and recent (20) room-temperature crystal structures at 2.01 to 2.27 Å resolution, we observe ~1,000 waters in each PS II monomer. The fact that these waters have electron density in the XFEL crystal structures at each state obtained at room temperature implies that they are structurally and functionally important for PS II. Our current results identified regions in the vicinity of the OEC where waters are less and more mobile based on the magnitude of observed positional changes of these waters between different illumination states (Fig. 6). We hypothesize that the former region (channel O4, channel Cl1) is important for proton release, and the latter (channel O1) may play a role in substrate water intake.

As reported earlier by Kern et al. (20), electron density of W20 disappears in the S_2 state. When present in S_1, this water is located close to the OEC in channel O4. We found that W20 is not visible in any of the structures measured during the $S_2 \rightarrow S_3$ transition. As W20 is already absent in the S_2 state it is not likely that W20 is the source of the substrate water that binds to the O_X position in the S_2–S_3 transition, contrary to some proposals (e.g., ref. 54 and *SI Appendix*, Fig. S1). Alternatively it was proposed that a change in the O4 channel involving W20 is connected to its role as a proton release path and that this channel could be active in the $S_0 \rightarrow S_1$ transition but not in the $S_2 \rightarrow S_3$ or $S_3 \rightarrow S_0$ transitions (20, 63). W19, located in the vicinity of W20 in the dark state (S_1), shows position changes between O4 and D1-S169. The shortest distance between W19 and O4 (2.4 Å) was observed in the S_2 state (1F). The displacement of W19 between the 0F and 1F states appears as a negative electron density in the isomorphous difference maps (Fig. 4), indicating a large shift in its position from the dark state (0F), corresponding to the shift of ~0.4 Å observed in the refined coordinates. We speculate that W19 takes a role of mediating proton movement between the OEC (O4) and the D61, S169, and R357 side chains, either for releasing protons from the OEC or compensating charges to avoid charging of the OEC.

Unlike waters in the O4 channel or the Cl1 channel, which have also been proposed as water channels (64–66), the waters along the O1 channel show significant positional changes during the $S_2 \rightarrow S_3$ transition (Fig. 6). A ring of five waters, W26–30 near O1 of the OEC located at the end of the O1 channel (Fig. 6 and *SI Appendix*, Fig. S10), could serve as an entrance for substrate water, shuffling water like a "water wheel" to the OEC. This idea is supported by the observation that concomitant to the O_X appearance, a significant negative electron density is seen near W27 during 150 to 400 μs after the second flash (Fig. 4*A*). Alternatively, the changes in water positions in this "water wheel" could play a role in charge compensation during the S-state advancement as suggested previously (20).

Recently Suga et al. (21) reported the appearance of a new water next to residue CP43-Val410 in their cryogenic 2F data in the region of the O1 channel. In our previous (20) and current room-temperature data we do not observe the occurrence of new water molecules in this region. Instead, the same region of electron density is explained by a double conformation of the side chain of residue CP43-Glu413, which is present both in the dark and in all of the illuminated states. It should be noted that instead of the glycerol molecules modeled in the cryogenic data (21), we observed several additional water molecules in this area. Some of these waters (e.g., W76 and W77) and surrounding amino acid side chains (e.g., V-Lys47, V-Tyr137, and CP43-Glu413) exhibit strong variability in position between the different illumination states, indicating a mobile region of the water network, consistent with the idea of the O1 channel's being an entrance for substrate water.

Possible Routes for O_X Insertion. Water insertion during the $S_2 \rightarrow S_3$ transition can be clearly followed by the buildup of the O_X density between Ca and Mn1. However, the origin of O_X, that is, from where and how the water reaches the O_X site and its protonation state once inserted remain open questions. Despite the interesting dynamics visible in the "water wheel" region of the O1 channel (discussed above), it is difficult to identify an exact water insertion route. This may indicate that the energetic barrier for water insertion is higher than for water transport to the OEC. There are four pathways that have been proposed in the literature (see *SI Appendix*, Fig. S1 for cases 2, 3, and 4): 1) W_{N1} (non-OEC ligated water near Mn1) → Mn1 (22), 2) W3 → Mn1 (28–30, 67), 3) W3 → Mn4 (14, 25, 28–30, 38, 68–71), or 4) W_{N2} (non-OEC ligated water near Mn4, for example W24 or W19) → Mn4 (36, 39, 72). In 1 and 2, water directly goes into the Mn1 open coordination site (O_X) and the OEC remains in the open-cubane configuration throughout the $S_2 \rightarrow S_3$ transition. In 3 and 4, on the other hand, water first binds as a ligand to Mn4 by shifting O5 toward Mn1 (i.e., a closed-cubane configuration), and this water shifts to the O5 position through flipping of bonds, thus the original O5 ending up at the O_X position in S_3 [pivot/carousel mechanism (36, 39, 72)].

Among the above four proposals, the $W_{N1} \rightarrow$ Mn1 pathway (case 1) is often disfavored due to steric hindrance of water movement to Mn1 caused by Val185 (69), unless this residue rotates at the water insertion event (22, 37). The density of the Val185 is, however, well-defined throughout the time point data we collected in this study and does not show any large motion. For water insertion to Mn4 (cases 3 or 4), it requires that the closed-cubane-like configuration forms prior to the formation of the S_3 state. As discussed above, the current results obtained by room temperature crystallography do not provide any evidence for the closed-cubane-like structure at any of the time points collected in this study. Based on the above observations, we hypothesize that water is inserted into the O_X site from W3 and refilled via the highly mobile waters in the O1 channel (case 2; see Fig. 7*B*). Chrysina et al. (35) recently reported an EPR signal that shows a small fraction of Mn(IV) in a highly distorted ligand environment in native PS II samples poised in the S_3 state. This signal was assigned by the authors as arising from either a five-coordinate Mn1(IV) within an open-cubane configuration or a five-coordinate Mn4(IV) within a closed-cubane configuration. Our data demonstrate that, at all times tested, the population of the proposed closed-cubane state, if present, cannot exceed our detection limit of 10% during the $S_2 \rightarrow S_3$ transition. Thus, we propose that a five-coordinate Mn1(IV) within an open-cubane conformation is a more likely intermediate during the $S_2 \rightarrow S_3$ transition.

Sequence of Events during the $S_2 \rightarrow S_3$ Transition. Fig. 7*A* summarizes the sequence of events that are observed around the OEC during the $S_2 \rightarrow S_3$ transition, based on crystallography and XES data. We show that collecting snapshot data at various time points at room temperature using XFELs allows for delineating the sequence of events that determine the directionality of the reaction, proceeding from one stable intermediate state to another, and providing a clear rationale for each transition. This combined crystallography and spectroscopy study correlates the structural changes occurring in the protein with the redox changes taking place at the metal center.

The earliest event we observe in this time-resolved study (Fig. 7*A*, *Top*) is the motion of Y_Z located between the primary donor, P_{680}, and the OEC, together with D1-His190-Asn298 residues, as well as the motion of D1-Glu189 next to Ca. This change occurs at <50 μs after the second light flash. These early changes can be explained by the transfer of an electron from Y_Z ($Y_Z \rightarrow Y_Z^{\bullet+}$) to $P_{680}^{\bullet+}$ immediately after the charge separation between P_{680}^{*} (excited state of P_{680}) and pheophytin. The oxidation of Y_Z is expected to change the H-bonding network along the residues D1-Y_Z-His190-Asn298 and the surrounding waters in their vicinity, while this process may also serve as a proton release pathway. Although we do not resolve it in this study at 50 μs, the changes at Glu189 will likely be preceded by the changes around Y_Z. Y_Z is located about 4 Å away from Glu189 and the formation of the positive charge at the Y_Z/His190 pair that precedes oxidation of the OEC could trigger structural changes in their surroundings, inducing a shift of Glu189 away from Ca as observed in the 2F(50 μs) data.

In the next step (<150 μs after the second flash; Fig. 7 *A*, *Middle*), the elongation of the Mn1–Mn4 distance is observed, while the Mn3–Mn4 pair maintains the di-μ-oxo bridged structure. We hypothesize that the proton release around Y_Z triggers the shift of the Mn4 and Mn1 positions in the early stage of the $S_2 \rightarrow S_3$ transition, which seems to be completed by ~150 μs. Subsequent to the Mn1–Mn4 motion, O_X becomes gradually

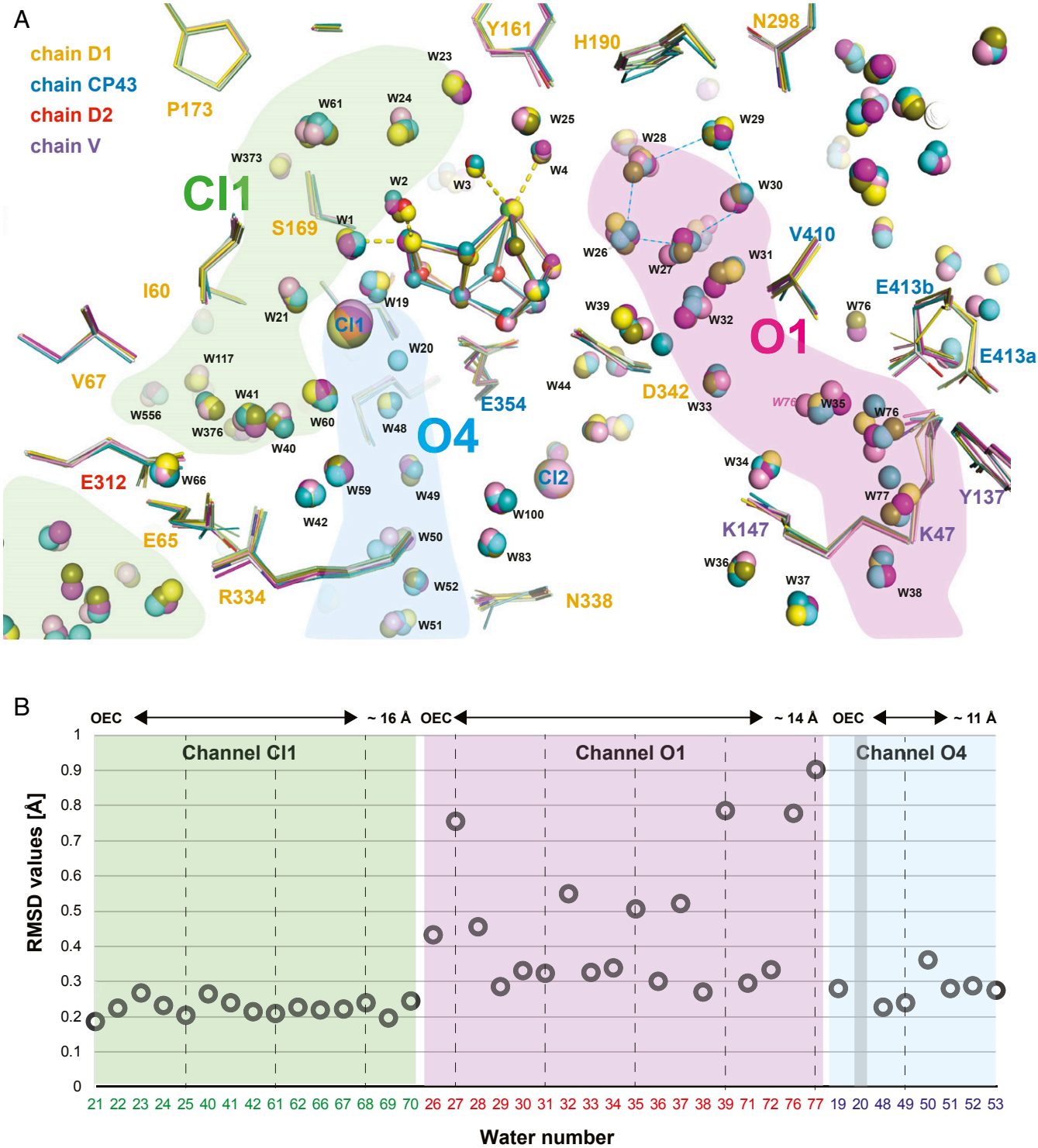

Fig. 6. The water network in the neighborhood of the OEC. (*A*) The structure of the protein and refined positions of waters surrounding the Mn_4Ca cluster are shown for monomer I for all time points [0F: gray; 1F: yellow; 2F(50 μs): pink; 2F(150 μs): cyan; 2F(250 μs): magenta; 2F(400 μs): green; 2F(200 ms): olive]. Residues are labeled according to subunit with D1 yellow, D2 red, CP43 blue, and PsbV magenta. Proposed channels connecting the OEC to the solvent-exposed surface of PS II for water movement or proton transfer are indicated in green, light blue, and pink. Oscillation of the cluster of five waters (W26–W30) in the proximity of O1 of the OEC is visible. (*B*) The rmsds of water positions (average over both monomers and all time points) within the vicinity of the Mn_4Ca cluster are shown as a function of their distance from the Mn_4Ca cluster. The waters in the O1 channel are more mobile on average than the waters in the Cl1 and O4 channels. As water 20 is only present in the 0F state but absent in the 1F and 2F states no rmsd for its position can be given. W39 is only present in one monomer and hence only the average over one monomer is given.

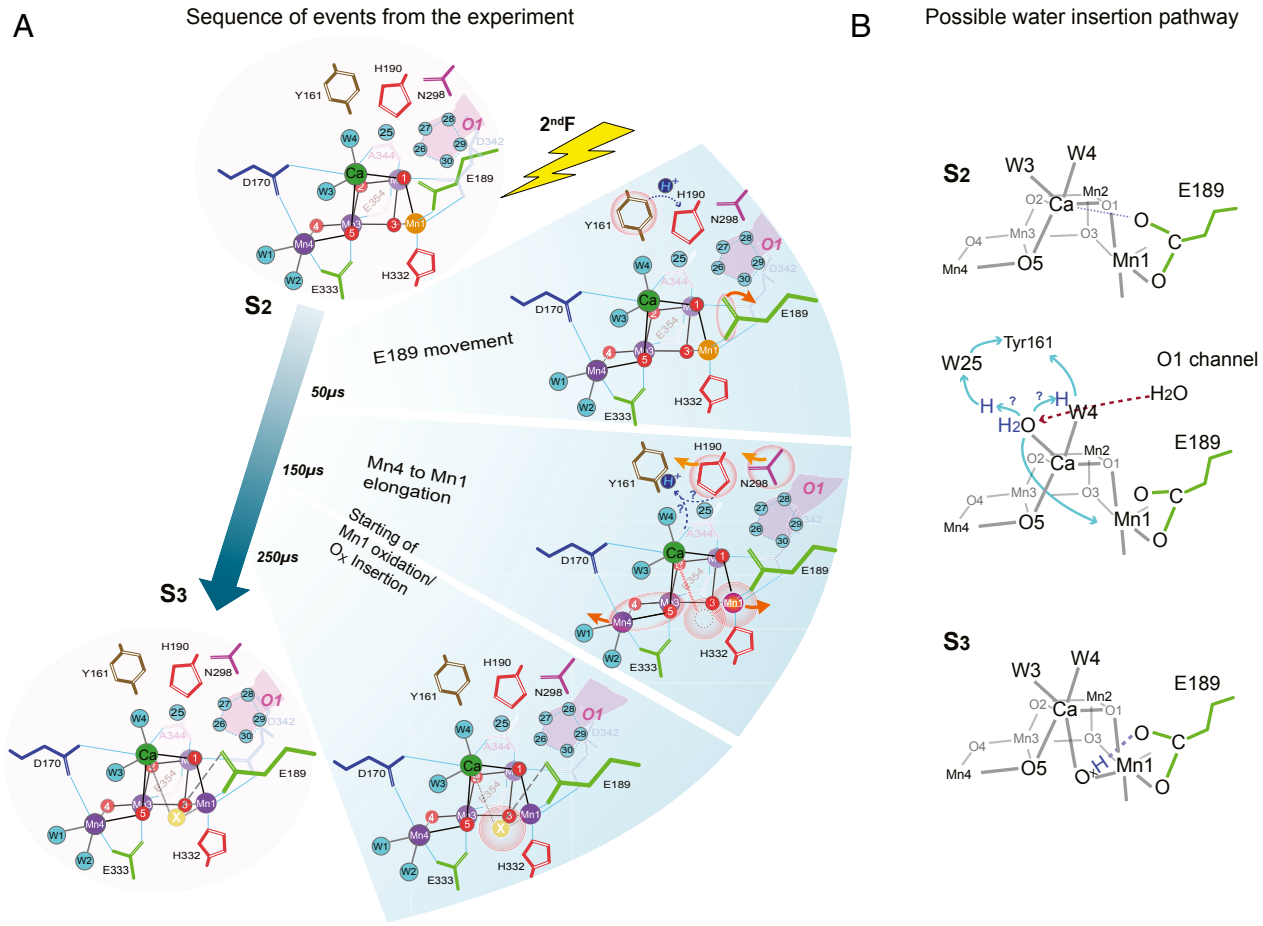

Fig. 7. Schematic of the $S_2 \rightarrow S_3$ transition. (*A*) The sequence of events in time leading to the insertion of O_X between Mn1 and Ca. Mn1 oxidation from (III) to (IV) is shown as a color change from orange to purple. The other Mn atoms are all in oxidation state (IV) and are shown in purple. Ca is shown in green. The ligands of Mn and Ca, Y_Z, and other neighboring residues and the water ligands of Mn4 and Ca are shown. Possible pathways for proton transfer are depicted as well. (*B*) Schematic showing possible water insertion from the O1 channel via W4/W3 to the O_X site and proton movements from W3 to Y_Z via W25 or W4. The protonated oxo bridge at the O_X position could form a hydrogen bond with the carboxylate chain of Glu189.

visible in the electron density maps; it is still within the noise level at 50 µs, but it is at ∼30% of its final occupancy by 150 µs, and ∼80% by 250 µs, and close to full occupancy by 400 µs (Fig. 7 *B*, *Bottom*). The oxidation of Mn1 appears to be directly coupled to the insertion of water, O_X, at the Mn1 open-coordination site into a bridging position between Ca and Mn1. Our previous XFEL data (20) as well as the current time-resolved data are consistent with this configuration.

How O_X arrives as a ligand to Mn1 in the S_3 state and what its protonation state is remain speculative at this point. However, we propose a hypothesis in Fig. 7*B* based on the OEC structural changes and the water and ligand motions experimentally observed in this study (Fig. 7*A*), as well as based on other experimental evidence reported in the literature. In the current study, we neither detected a closed-cubane-like structure nor a change in the Mn3–Mn4 moiety, both features that may be necessary prerequisites for indicating a water (O_X) insertion pathway that involves Mn4. Therefore, we hypothesize that O_X does not originate from a ligand of Mn4 but is derived from the Ca-bound water W3.

Several studies have proposed that Ca-bound water (W3) may serve as the entrance point for substrate water (see, e.g., refs. 28, 30, 54, and 73). For example, FTIR studies showed changes in water vibrational modes during the $S_2 \rightarrow S_3$ transition that are sensitive to the substitution of Ca with Sr (14, 28, 68, 70), and these modes were assigned to Ca-bound W3. We also proposed in our recent study that W3 could serve as an entry point for substrate water (20). The high mobility of waters in the O1 channel, especially in the region of the "water wheel" observed in this study (Figs. 6 and 7*A*), supports the hypothesis that the substrate water likely arrives from the O1 channel. The pathway of water from the "water wheel" to W3 is likely via W4 (Fig. 7 *B*, *Middle*). If the insertion of the water occurs from the W3 site, this could be triggered by the oxidation of Y_Z and the proton transfer to the neighboring His190 (Y_Z^{ox}-His190$^+$ formation), because it reduces the pK_a of W3. Then, upon oxidation of the Mn cluster [five coordinate Mn1(III) → five coordinate Mn1(IV)] and reduction of $Y_Z^{\bullet}$, the tyrosine could accept the proton indirectly (e.g., via W4 or W25) from W3, leading to formation of a hydroxide that is concomitantly transferred to the open coordination site of Mn1(IV) (30). In the current study, we show that the oxidation of Mn and water (O_X) binding are highly correlated events, but we cannot distinguish the exact order of these two events within the current time resolution and signal-to-noise ratio of XES and crystallography data. The noticeable shift in the first moment of the X-ray emission spectra at 50 µs after the second flash (Fig. 5*C* and *SI Appendix*, Fig. S8) could suggest that Mn oxidation triggers O_X insertion, although the data are also compatible with a faster structural rearrangement process that does not change the oxidation state of the Mn_4Ca cluster followed by concomitant Mn oxidation and O_X insertion. Most theoretical studies have proposed a concerted mechanism that requires binding of water first before Mn oxidation. However, recently Chrysina

et al. (35), based on W-band EPR results, proposed oxidation of Mn1 prior to binding of water, which would also be consistent with our results presented above.

It has been proposed that an O5–O_X (or O6) peroxo-bond may form already in the S_3 state (19). We clearly showed previously and confirm in the current study that no O5–O_X bond is formed in the S_3 state or any of the time points during the $S_2 \rightarrow S_3$ transition. Moreover, our XES results do not show a reduction of Mn in the S_3 state, that should accompany any formation of an O–O peroxo-bond. Instead, our data clearly show that O_X is a bridging ligand between Ca and Mn1, and we propose that O_X is hydrogen-bonded to the carboxylate oxygen of Glu189 located at a distance of 2.4 Å (Fig. 7 *B*, *Bottom*). We note that O_X has been proposed as a hydroxide ligand based on EPR data and theoretical studies (23, 37, 40, 67), satisfying the S = 3 spin state configuration assigned for the S_3 state.

The current study demonstrates that untangling the structural sequence of events during the transition from one intermediate state to another in a time-resolved manner provides mechanistic insights into how the photochemically induced reactions proceed at the donor and acceptor sides. These studies take us one step closer to understanding the even more complex and highly orchestrated chemical process that is expected during the $S_3 \rightarrow S_0$ transition in PS II. In this transition the catalytic center is first oxidized one more step by the absorption of another photon, which is followed by a cascade of events that includes the release of two protons the O–O bond formation, release of O_2 and the binding of one water, resetting the chemistry for the next catalytic cycle.

Methods

Dimeric PS II was extracted and purified from *T. elongatus* and crystallized as described previously (18, 20). Activity and intactness of the samples used was confirmed by O_2 evolution measurements using a Clark-type electrode, by EPR measurements to assay for Mn(II), and by membrane inlet mass spectrometric measurements of O_2 production. Based on these measurements the S-state population for different illumination states was determined (*SI Appendix*, Table S2). Acoustic droplet ejection together with a drop on tape setup (74) was utilized to perform SFX and XES experiments at both the LCLS and SACLA XFEL facilities (59, 60). Illumination of samples was achieved using nanosecond-length pulses at 532/527 nm from Nd:YAG or Nd:YLF lasers with timing of 0.2 s between individual illumination pulses for generation of steady states and variable timing (50 to 400 μs), between the final illumination and X-ray probing for 2F(time point) data collection. SFX data were collected using a Rayonix MX340-XFEL or an octal MPCCD detector. XES signal was collected by means of a 16 analyzer crystal array in van Hamos geometry together with an ePIX 100 or a single module MPCCD detector (75). SFX data processing used the cctbx.xfel software framework (41, 76). Crystallographic model building, refinement and map calculation was performed with Phenix (77) and Coot (78) and figures were generated using PyMol (79). END/RAPID (56) was used to derive error estimates for distances. Detailed protocols can be found in *SI Appendix, Methods*.

Data Availability. X-ray diffraction datasets and associated models have been deposited in the Research Collaboratory for Structural Bioinformatics (RCSB) Protein Data Bank (https://www.rcsb.org) under PDB ID codes 6W1O for the 0F, 6W1P for the 1F, 6W1Q for the 2F(50 μs), 6W1R for the 2F(150 μs), 6W1T for the 2F(250 μs), 6W1U for the 2F(400 μs), and 6W1V for the 2F(200 ms) data.

ACKNOWLEDGMENTS. We thank Gesine Bartels and Julia Wersig for technical support. This work was supported by the Director, Office of Science, Office of Basic Energy Sciences (OBES), Division of Chemical Sciences, Geosciences, and Biosciences of the Department of Energy (DOE) (J.Y. and V.K.Y.) for X-ray methodology and instrumentation and spectroscopy and crystallography data collection and analysis by NIH grants GM055302 (V.K.Y.) for PS II biochemistry, GM110501 (J.Y.) and GM126289 (J.K.) for instrumentation development for XFEL experiments, and GM117126 (N.K.S.) for development of computational protocols for XFEL data. NIH grants GM133081 (K.D.S.), GM124149, and GM124169 (J.M.H.) and Vetenskapsrådet 2016-05183 (J.M.) and 2017-00356 (T.F.) are acknowledged for support. Funding was also provided by the Deutsche Forschungsgemeinschaft under Germany's Excellence Strategy – grants EXC 2008/1 – 390540038 (Gesine Bartels) and Sfb1078 (Humboldt Universität Berlin), TP A5 (A.Z., H.D., R.H., M.I., and Julia Wersig). A.M.O. was supported in part by Diamond Light Source and A.M.O. acknowledges support from a Strategic Award from the Wellcome Trust and the Biotechnology and Biological Sciences Research Council (grant 102593), a Wellcome Investigator Award in Science (210734/Z/18/Z), and a Royal Society Wolfson Fellowship (RSWF\R2\182017). This research used resources of the National Energy Research Scientific Computing Center, a User Facility supported by the Office of Science, DOE, under contract DE-AC02-05CH11231. XFEL data were collected at LCLS/SLAC, Stanford and under proposal 2018B8089 at SACLA, Japan. Testing of crystals and various parts of the setup were carried out at synchrotron facilities that were provided by the Advanced Light Source (ALS) in Berkeley and Stanford Synchrotron Radiation Lightsource (SSRL) in Stanford, funded by DOE OBES, and PL14 at Berliner Elektronenspeicherring-Gesellschaft für Synchrotronstrahlung (BESSY-II), Berlin. The SSRL Structural Molecular Biology Program is supported by the DOE OBER and by the NIH (grant P41GM103393). Use of the LCLS and SSRL, SLAC National Accelerator Laboratory, is supported by the US DOE, Office of Science, OBES under contract DE-AC02-76SF00515. The Rayonix detector used at LCLS was supported by the NIH grant S10 OD023453. We thank the support staff at LCLS/SLAC, SACLA, and SSRL (beamlines 6-2, 7-3) and ALS (beamlines 5.0.1, 5.0.2, 8.2.1, and 8.3.1).

1. P. Joliot, G. Barbieri, R. Chabaud, A new model of photochemical centers in system-2. *Photochem. Photobiol.* **10**, 309–329 (1969).
2. B. Kok, B. Forbush, M. McGloin, Cooperation of charges in photosynthetic O_2 evolution-I. A linear four step mechanism. *Photochem. Photobiol.* **11**, 457–475 (1970).
3. F. Rappaport, B. A. Diner, Primary photochemistry and energetics leading to the oxidation of the Mn_4Ca cluster and to the evolution of molecular oxygen in photosystem II. *Coord. Chem. Rev.* **252**, 259–272 (2008).
4. F. Müh, C. Glöckner, J. Hellmich, A. Zouni, Light-induced quinone reduction in photosystem II. *Biochim. Biophys. Acta* **1817**, 44–65 (2012).
5. S. Itoh, C. T. Yerkes, H. Koike, H. H. Robinson, A. R. Crofts, Effects of chloride depletion on electron donation from the water-oxidizing complex to the photosystem II reaction center as measured by the microsecond rise of chlorophyll fluorescence in isolated pea-chloroplasts. *Biochim. Biophys. Acta* **766**, 612–622 (1984).
6. S. M. Theg, P. A. Jursinic, P. H. Homann, Studies on the mechanism of chloride action on photosynthetic water oxidation. *Biochim. Biophys. Acta* **766**, 636–646 (1984).
7. A. Boussac, A. W. Rutherford, S-state formation after Ca^{2+} depletion in the photosystem II oxygen-evolving complex. *Chem. Scr.* **28A**, 123–126 (1988).
8. A. Boussac, A. W. Rutherford, Nature of the inhibition of the oxygen-evolving enzyme of photosystem II induced by NaCl washing and reversed by the addition of Ca^{2+} or Sr^{2+}. *Biochemistry* **27**, 3476–3483 (1988).
9. M. Karge, K.-D. Irrgang, G. Renger, Analysis of the reaction coordinate of photosynthetic water oxidation by kinetic measurements of 355 nm absorption changes at different temperatures in photosystem II preparations suspended in either H_2O or D_2O. *Biochemistry* **36**, 8904–8913 (1997).
10. R. J. Debus, Protein ligation of the photosynthetic oxygen-evolving center. *Coord. Chem. Rev.* **252**, 244–258 (2008).
11. G. Renger, P. Kühn, Reaction pattern and mechanism of light induced oxidative water splitting in photosynthesis. *Biochim. Biophys. Acta* **1767**, 458–471 (2007).
12. J. Messinger, W. P. Schröder, G. Renger, Structure-function relations in photosystem II. Effects of temperature and chaotropic agents on the period four oscillation of flash-induced oxygen evolution. *Biochemistry* **32**, 7658–7668 (1993).
13. J. Messinger, U. Wacker, G. Renger, Unusual low reactivity of the water oxidase in redox state S_3 toward exogenous reductants. Analysis of the NH_2OH and NH_2NH_2 induced modifications of flash-induced oxygen evolution in isolated spinach thylakoids. *Biochemistry* **30**, 7852–7862 (1991).
14. H. Suzuki, M. Sugiura, T. Noguchi, Monitoring water reactions during the S-state cycle of the photosynthetic water-oxidizing center: Detection of the DOD bending vibrations by means of Fourier transform infrared spectroscopy. *Biochemistry* **47**, 11024–11030 (2008).
15. J. Kern *et al.*, Simultaneous femtosecond X-ray spectroscopy and diffraction of photosystem II at room temperature. *Science* **340**, 491–495 (2013).
16. J. Kern *et al.*, Taking snapshots of photosynthetic water oxidation using femtosecond X-ray diffraction and spectroscopy. *Nat. Commun.* **5**, 4371 (2014).
17. C. Kupitz *et al.*, Serial time-resolved crystallography of photosystem II using a femtosecond X-ray laser. *Nature* **513**, 261–265 (2014).
18. I. D. Young *et al.*, Structure of photosystem II and substrate binding at room temperature. *Nature* **540**, 453–457 (2016).
19. M. Suga *et al.*, Light-induced structural changes and the site of O=O bond formation in PSII caught by XFEL. *Nature* **543**, 131–135 (2017).
20. J. Kern *et al.*, Structures of the intermediates of Kok's photosynthetic water oxidation clock. *Nature* **563**, 421–425 (2018).
21. M. Suga *et al.*, An oxyl/oxo mechanism for oxygen-oxygen coupling in PSII revealed by an x-ray free-electron laser. *Science* **366**, 334–338 (2019).
22. P. E. M. Siegbahn, Structures and energetics for O_2 formation in photosystem II. *Acc. Chem. Res.* **42**, 1871–1880 (2009).
23. N. Cox *et al.*, Photosynthesis. Electronic structure of the oxygen-evolving complex in photosystem II prior to O-O bond formation. *Science* **345**, 804–808 (2014).

24. M. Shoji, H. Isobe, K. Yamaguchi, QM/MM study of the S_2 to S_3 transition reaction in the oxygen-evolving complex of photosystem II. *Chem. Phys. Lett.* **636**, 172–179 (2015).
25. D. Bovi, D. Narzi, L. Guidoni, The S_2 state of the oxygen-evolving complex of photosystem II explored by QM/MM dynamics: Spin surfaces and metastable states suggest a reaction path towards the S_3 state. *Angew. Chem. Int. Ed. Engl.* **52**, 11744–11749 (2013).
26. H. Isobe *et al*., Theoretical illumination of water-inserted structures of the $CaMn_4O_5$ cluster in the S_2 and S_3 states of oxygen-evolving complex of photosystem II: Full geometry optimizations by B3LYP hybrid density functional. *Dalton Trans.* **41**, 13727–13740 (2012).
27. D. A. Pantazis, The S_3 state of the oxygen-evolving complex: Overview of spectroscopy and XFEL crystallography with a critical evaluation of early-onset models for O–O bond formation. *Inorganics* **7**, 55 (2019).
28. C. J. Kim, R. J. Debus, One of the substrate waters for O_2 formation in photosystem II is provided by the water-splitting Mn_4CaO_5 cluster's Ca^{2+} Ion. *Biochemistry* **58**, 3185–3192 (2019).
29. H. Sakamoto, T. Shimizu, R. Nagao, T. Noguchi, Monitoring the reaction process during the $S_2 \rightarrow S_3$ transition in photosynthetic water oxidation using time-resolved infrared spectroscopy. *J. Am. Chem. Soc.* **139**, 2022–2029 (2017).
30. I. Ugur, A. W. Rutherford, V. R. Kaila, Redox-coupled substrate water reorganization in the active site of photosystem II-The role of calcium in substrate water delivery. *Biochim. Biophys. Acta* **1857**, 740–748 (2016).
31. W. Ames *et al*., Theoretical evaluation of structural models of the S_2 state in the oxygen evolving complex of photosystem II: Protonation states and magnetic interactions. *J. Am. Chem. Soc.* **133**, 19743–19757 (2011).
32. P. E. M. Siegbahn, O-O bond formation in the S_4 state of the oxygen-evolving complex in photosystem II. *Chemistry* **12**, 9217–9227 (2006).
33. A. Klauss, M. Haumann, H. Dau, Seven steps of alternating electron and proton transfer in photosystem II water oxidation traced by time-resolved photothermal beam deflection at improved sensitivity. *J. Phys. Chem. B* **119**, 2677–2689 (2015).
34. A. Klauss, M. Haumann, H. Dau, Alternating electron and proton transfer steps in photosynthetic water oxidation. *Proc. Natl. Acad. Sci. U.S.A.* **109**, 16035–16040 (2012).
35. M. Chrysina *et al*., Five-coordinate Mn^{IV} intermediate in the activation of nature's water splitting cofactor. *Proc. Natl. Acad. Sci. U.S.A.* **116**, 16841–16846 (2019).
36. M. Retegan *et al*., A five-coordinate Mn(IV) intermediate in biological water oxidation: Spectroscopic signature and a pivot mechanism for water binding. *Chem. Sci.* **7**, 72–84 (2016).
37. P. E. M. Siegbahn, The S_2 to S_3 transition for water oxidation in PSII (photosystem II), revisited. *Phys. Chem. Chem. Phys.* **20**, 22926–22931 (2018).
38. M. Capone, D. Narzi, D. Bovi, L. Guidoni, Mechanism of water delivery to the active site of photosystem II along the S_2 to S_3 transition. *J. Phys. Chem. Lett.* **7**, 592–596 (2016).
39. M. Askerka, J. Wang, D. J. Vinyard, G. W. Brudvig, V. S. Batista, S_3 state of the O_2-evolving complex of photosystem II: Insights from QM/MM, EXAFS, and femtosecond X-ray diffraction. *Biochemistry* **55**, 981–984 (2016).
40. D. A. Pantazis, W. Ames, N. Cox, W. Lubitz, F. Neese, Two interconvertible structures that explain the spectroscopic properties of the oxygen-evolving complex of photosystem II in the S_2 state. *Angew. Chem. Int. Ed. Engl.* **51**, 9935–9940 (2012).
41. A. S. Brewster *et al*., Improving signal strength in serial crystallography with DIALS geometry refinement. *Acta Crystallogr. D Struct. Biol.* **74**, 877–894 (2018).
42. K. Hasegawa, T. Noguchi, Molecular interactions of the quinone electron acceptors Q_A, Q_B, and Q_C in photosystem II as studied by the fragment molecular orbital method. *Photosynth. Res.* **120**, 113–123 (2014).
43. K. Zimmermann *et al*., Herbicide binding and thermal stability of photosystem II isolated from *Thermosynechococcus elongatus*. *Biochim. Biophys. Acta* **1757**, 106–114 (2006).
44. T. Noguchi, H. Suzuki, M. Tsuno, M. Sugiura, C. Kato, Time-resolved infrared detection of the proton and protein dynamics during photosynthetic oxygen evolution. *Biochemistry* **51**, 3205–3214 (2012).
45. R. Krivanek, J. Kern, A. Zouni, H. Dau, M. Haumann, Spare quinones in the Q_B cavity of crystallized photosystem II from *Thermosynechococcus elongatus*. *Biochim. Biophys. Acta* **1767**, 520–527 (2007).
46. B. A. Barry, G. T. Babcock, Tyrosine radicals are involved in the photosynthetic oxygen-evolving system. *Proc. Natl. Acad. Sci. U.S.A.* **84**, 7099–7103 (1987).
47. M. L. Gilchrist, Jr., J. A. Ball, D. W. Randall, R. D. Britt, Proximity of the manganese cluster of photosystem II to the redox-active tyrosine Y_Z. *Proc. Natl. Acad. Sci. U.S.A.* **92**, 9545–9549 (1995).
48. R. Ahlbrink *et al*., Function of tyrosine Z in water oxidation by photosystem II: Electrostatical promotor instead of hydrogen abstractor. *Biochemistry* **37**, 1131–1142 (1998).
49. G. T. Babcock, R. E. Blankenship, K. Sauer, Reaction kinetics for positive charge accumulation on the water side of chloroplast photosystem II. *FEBS Lett.* **61**, 286–289 (1976).
50. M. Boska, K. Sauer, Kinetics of EPR signal II_{vf} in chloroplast photosystem II. *BBA-Bioenergetics* **765**, 84–87 (1984).
51. P. Kühn, H. Eckert, H. J. Eichler, G. Renger, Analysis of the $P680^{+\cdot}$ reduction pattern and its temperature dependence in oxygen-evolving PSII core complexes from a thermophilic cyanobacteria and higher plants. *Phys. Chem. Chem. Phys.* **6**, 4838–4843 (2004).
52. Y. Umena, K. Kawakami, J.-R. Shen, N. Kamiya, Crystal structure of oxygen-evolving photosystem II at a resolution of 1.9 Å. *Nature* **473**, 55–60 (2011).
53. R. Nagao, H. Ueoka-Nakanishi, T. Noguchi, D1-Asn-298 in photosystem II is involved in a hydrogen-bond network near the redox-active tyrosine Y_Z for proton exit during water oxidation. *J. Biol. Chem.* **292**, 20046–20057 (2017).
54. M. Askerka, G. W. Brudvig, V. S. Batista, The O_2-evolving complex of photosystem II: Recent insights from quantum mechanics/molecular mechanics (QM/MM), extended X-ray absorption fine structure (EXAFS), and femtosecond X-ray crystallography data. *Acc. Chem. Res.* **50**, 41–48 (2017).
55. T. A. Corry, P. J. O'Malley, Proton isomers rationalize the high- and low-spin forms of the S_2 state intermediate in the water-oxidizing reaction of photosystem II. *J. Phys. Chem. Lett.* **10**, 5226–5230 (2019).
56. P. T. Lang, J. M. Holton, J. S. Fraser, T. Alber, Protein structural ensembles are revealed by redefining X-ray electron density noise. *Proc. Natl. Acad. Sci. U.S.A.* **111**, 237–242 (2014).
57. I. Zaharieva *et al*., Room-temperature energy-sampling Kβ X-ray emission spectroscopy of the Mn_4Ca complex of photosynthesis reveals three manganese-centered oxidation steps and suggests a coordination change prior to O_2 formation. *Biochemistry* **55**, 4197–4211 (2016).
58. T. Ishikawa *et al*., A compact X-ray free-electron laser emitting in the sub-Ångstrom region. *Nat. Photonics* **6**, 540–544 (2012).
59. K. Tono *et al*., Beamline, experimental stations and photon beam diagnostics for the hard x-ray free electron laser of SACLA. *New J. Phys.* **15**, 83025 (2013).
60. R. G. Sierra *et al*., The Macromolecular Femtosecond Crystallography instrument at the Linac Coherent Light Source. *J. Synchrotron Radiat.* **26**, 346–357 (2019).
61. P. Emma *et al*., First lasing and operation of an Ångstrom-wavelength free-electron laser. *Nat. Photonics* **4**, 641–647 (2010).
62. I. Zaharieva, H. Dau, M. Haumann, Sequential and coupled proton and electron transfer events in the $S_2 \rightarrow S_3$ transition of photosynthetic water oxidation revealed by time-resolved X-ray absorption spectroscopy. *Biochemistry* **55**, 6996–7004 (2016).
63. K. Saito, A. W. Rutherford, H. Ishikita, Energetics of proton release on the first oxidation step in the water-oxidizing enzyme. *Nat. Commun.* **6**, 8488 (2015).
64. F. M. Ho, Uncovering channels in photosystem II by computer modelling: Current progress, future prospects, and lessons from analogous systems. *Photosynth. Res.* **98**, 503–522 (2008).
65. A. Gabdulkhakov *et al*., Probing the accessibility of the Mn_4Ca cluster in photosystem II: Channels calculation, noble gas derivatization, and cocrystallization with DMSO. *Structure* **17**, 1223–1234 (2009).
66. S. Vassiliev, T. Zaraiskaya, D. Bruce, Exploring the energetics of water permeation in photosystem II by multiple steered molecular dynamics simulations. *Biochim. Biophys. Acta* **1817**, 1671–1678 (2012).
67. K. Yamaguchi *et al*., Theoretical and computational investigations of geometrical, electronic and spin structures of the $CaMn_4O_X$ (X = 5, 6) cluster in the Kok cycle S_i (i = 0-3) of oxygen evolving complex of photosystem II. *Physiol. Plant.* **166**, 44–59 (2019).
68. T. Noguchi, FTIR detection of water reactions in the oxygen-evolving centre of photosystem II. *Philos. Trans. R. Soc. B* **363**, 1189–1195 (2008).
69. C. J. Kim, H. Bao, R. L. Burnap, R. J. Debus, Impact of D1-V185 on the water molecules that facilitate O_2 formation by the catalytic Mn_4CaO_5 cluster in photosystem II. *Biochemistry* **57**, 4299–4311 (2018).
70. C. J. Kim, R. J. Debus, Evidence from FTIR difference spectroscopy that a substrate H_2O molecule for O_2 formation in photosystem II Is provided by the Ca ion of the catalytic Mn_4CaO_5 cluster. *Biochemistry* **56**, 2558–2570 (2017).
71. M. Capone, D. Bovi, D. Narzi, L. Guidoni, Reorganization of substrate waters between the closed and open cubane conformers during the S_2 to S_3 transition in the oxygen evolving complex. *Biochemistry* **54**, 6439–6442 (2015).
72. M. Askerka, D. J. Vinyard, G. W. Brudvig, V. S. Batista, NH_3 binding to the S_2 state of the O_2-evolving complex of photosystem II: Analogue to H_2O binding during the $S_2 \rightarrow S_3$ transition. *Biochemistry* **54**, 5783–5786 (2015).
73. J. Tso, M. Sivaraja, G. C. Dismukes, Calcium limits substrate accessibility or reactivity at the manganese cluster in photosynthetic water oxidation. *Biochemistry* **30**, 4734–4739 (1991).
74. F. D. Fuller *et al*., Drop-on-demand sample delivery for studying biocatalysts in action at XFELs. *Nat. Methods* **14**, 443–449 (2017).
75. T. Fransson *et al*., X-ray emission spectroscopy as an in situ diagnostic tool for X-ray crystallography of metalloproteins using an X-ray free-electron laser. *Biochemistry* **57**, 4629–4637 (2018).
76. N. K. Sauter, XFEL diffraction: Developing processing methods to optimize data quality. *J. Synchrotron Radiat.* **22**, 239–248 (2015).
77. D. Liebschner *et al*., Macromolecular structure determination using X-rays, neutrons and electrons: recent developments in Phenix. *Acta Crystallogr. D Biol. Crystallogr.* **75**, 861–877 (2019).
78. P. Emsley, B. Lohkamp, W. G. Scott, K. Cowtan, Features and development of Coot. *Acta Crystallogr. D Biol. Crystallogr.* **66**, 486–501 (2010).
79. Schrödinger LLC, The PyMOL Molecular Graphics System (Version 1.8., Schrödinger LLC, 2015).